PROTOCLUSTER DISCOVERY IN TOMOGRAPHIC LYα FOREST FLUX MAPS

Casey W. Stark[1], Martin White[1,2,3], Khee-Gan Lee[4], Joseph F. Hennawi[4]
[1] Department of Astronomy, University of California, Berkeley, CA 94720, USA
[2] Department of Physics, University of California, Berkeley, CA 94720, USA
[3] Lawrence Berkeley National Laboratory, 1 Cyclotron Road, Berkeley, CA 93720, USA
[4] Max Planck Institute for Astronomy, Königstuhl 17, D-69117 Heidelberg, West Germany
Draft version March 5, 2018

ABSTRACT

We present a new method of finding protoclusters using tomographic maps of Lyα Forest flux. We review our method of creating tomographic flux maps and discuss our new high performance implementation, which makes large reconstructions computationally feasible. Using a large N-body simulation, we illustrate how protoclusters create large-scale flux decrements, roughly $10\,h^{-1}\mathrm{Mpc}$ across, and how we can use this signal to find them in flux maps. We test the performance of our protocluster finding method by running it on the ideal, noiseless map and tomographic reconstructions from mock surveys, and comparing to the halo catalog. Using the noiseless map, we find protocluster candidates with about 90% purity, and recover about 75% of the protoclusters that form massive clusters ($> 3 \times 10^{14}\,h^{-1}M_\odot$). We construct mock surveys similar to the ongoing COSMOS Lyman-Alpha Mapping And Tomography Observations (CLAMATO) survey. While the existing data has an average sightline separation of $2.3\,h^{-1}\mathrm{Mpc}$, we test separations of $2 - 6\,h^{-1}\mathrm{Mpc}$ to see what can be tolerated for our application. Using reconstructed maps from small separation mock surveys, the protocluster candidate purity and completeness are very close to what was found in the noiseless case. As the sightline separation increases, the purity and completeness decrease, although they remain much higher than we initially expected. We extended our test cases to mock surveys with an average separation of $15\,h^{-1}\mathrm{Mpc}$, meant to reproduce high source density areas of the BOSS survey. We find that even with such a large sightline separation, the method can still be used to find some of the largest protoclusters.

1. INTRODUCTION

Galaxy clusters are the largest and most massive gravitationally-bound structures in the Universe, the endpoint of a long process of hierarchical structure formation. Due to their large mass, deep potential wells and dynamic formation histories they are important laboratories for studying galaxy evolution, plasma physics, and our models of gravity and cosmology (Fabian 1994; Kravtsov & Borgani 2012; Feretti et al. 2012). Despite keen interest in how clusters form, the study of early cluster formation, at high z, is observationally limited: clusters are rare and surveying large volumes is expensive. Indeed, the total comoving volume of even the largest surveys for distant galaxies at $z \sim 2 - 3$ (e.g. KBSS, Rudie et al. 2012) is only $\sim 10^7\,\mathrm{Mpc}^3$, which would barely contain a single rich cluster locally. In the past decade small samples of protoclusters have been compiled (see e.g. Chiang et al. 2013, 2014, for a recent compilation) but important questions regarding the formation of clusters and the evolutionary tracks of member galaxies remain unresolved (e.g. Peterson & Fabian 2006; Dolag et al. 2009; Martizzi et al. 2014). There has been progress in the theoretical understanding of cluster formation through the use of N-body simulations and semi-analytic galaxy formation models (Baugh 2006; Benson & Bower 2010; Benson 2012) and hydrodynamical simulations (Sijacki & Springel 2006; McCarthy et al. 2010; Yang et al. 2012; Skory et al. 2013; Vogelsberger et al. 2013; Genel et al. 2014), although it is a notoriously difficult problem to predict member galaxy properties from

first principles. It is an area of ongoing research to validate and extend the numerous assumptions and subgrid recipes which are made in these works.

With the advent of large surveys in the optical and near-IR (Postman et al. 1996; Kochanek et al. 2003; Gladders & Yee 2005; Koester et al. 2007; Wilson et al. 2009; Muzzin et al. 2009; Hao et al. 2010; Szabo et al. 2011; Murphy et al. 2012; Rykoff et al. 2014; Bleem et al. 2014), sub-mm (Marriage et al. 2011; Reichardt et al. 2013; Planck Collaboration et al. 2013b) and X-ray (Ebeling et al. 2000; Böhringer et al. 2004; Burenin et al. 2007; Pierre et al. 2006; Finoguenov et al. 2007) bands we now have large samples of clusters, with a tail extending beyond $z \simeq 1 - 2$. These surveys leverage the fact that 'mature' clusters contain large overdensities of (typically red) galaxies and a hot intracluster medium. Protoclusters, at $z = 2$ or earlier, lack these signatures making them more difficult to find and study. At the time of writing only a few tens of protocluster candidates are known at $z > 2$ (see Chiang et al. 2013, 2014; Finley et al. 2014; Cucciati et al. 2014), and most candidates were found via the the signpost technique, i.e. using a radio-galaxy, Lyα blob, or another source as a marker.

Assuming a mean interior density of 200 times the background density, the linear size of the mean-density region from which material is accreted into a halo should be about $5 - 6$ times the virial radius of the final halo. For protoclusters this can be up to $10\,h^{-1}\mathrm{Mpc}$, i.e. we expect that the $z \sim 2$ progenitors of massive clusters should lie in overdense regions many (comoving) Mpc in radius. This expectation is born out of numerical simulations

(e.g. Chiang et al. 2013) which also show that the most massive clusters today form not from the most overdense regions at high z but from large, possibly only moderately overdense regions (Angulo et al. 2012). The progenitor regions of massive low-z clusters should thus be identifiable in relatively low-resolution large-scale structure maps of the high-z Universe. Systematic searches in large, deep, galaxy redshift surveys or multi-band photometric surveys are one promising way to find protoclusters (e.g. Chiang et al. 2014; Diener et al. 2014; Yuan et al. 2014), although projection effects pose a challenging problem. Spectroscopic surveys with sufficient sampling of Mpc-scales take care of this problem, although redshift errors can still be significant and covering large volumes with such high resolution is prohibitively expensive.

An alternative is tomographic mapping using Lyα absorption from neutral Hydrogen in the intergalactic medium (IGM) (Caucci et al. 2008; Cai et al. 2014; Lee et al. 2014a). Lee et al. (2014a) demonstrated that IGM tomography allows large volumes of the Universe to be efficiently searched for protoclusters in the $z \simeq 2$ – 3 range using existing facilities. By targeting star-forming Lyman-break galaxies (LBGs) as well as quasars at $g \gtrsim 24.5$, at signal-to-noise ratios achievable with existing facilities, we can obtain hundreds of sightlines per deg^2. This sightline density corresponds to average spacings of several Mpc, which is also the correlation scale of the Lyα forest. By sampling the IGM absorption along and across sightlines with Mpc spacing, we are able to tomographically reconstruct the 3D Lyα forest flux field. These tomographic maps have a resolution similar to the average transverse sightline spacing and naturally avoid projection effects or redshift errors. In Lee et al. (2014c), we constructed a tomographic IGM map using 24 LBG spectra with an average sightline separation $\langle d_\perp \rangle = 2.3\,h^{-1}$Mpc, obtained with two 2-hour exposures on Keck LRIS. These observations made up the pilot data of the COSMOS Lyman-Alpha Mapping And Tomography Observations (CLAMATO) survey, which we plan to extend to cover 1 deg^2. These observations will result in a tomographic map with a volume of roughly $70 \times 70 \times 230\,h^{-1}$Mpc and $2\,h^{-1}$Mpc resolution. Such a map will provide an unprecedented view of the intergalactic medium and provide a large volume to search for protoclusters.

Given the diversity of protoclusters, the ability to construct large samples is important if we are to draw robust conclusions about cluster formation. Optical, sub-mm and X-ray facilities could then be used to follow up the most promising candidates looking for galaxy over densities, Compton decrements or faint, diffuse X-ray emission. The HETDEX (Hill et al. 2004) and Subaru Prime Focus (Takada et al. 2014) spectrographs would be particularly powerful for following up such candidates in the optical. As we shall show later, the most massive progenitors of the most massive clusters today $(M > 3 \times 10^{14}\,h^{-1}M_\odot)$ can reach the rich group scale $(M \sim 3 \times 10^{13}\,h^{-1}M_\odot)$ before $z \sim 2$. Such structures could well have observable galaxy overdensities and a hot gas component at early times.

The outline of the paper is as follows. In Section 2 we introduce the numerical simulation we use to study pro-

tocluster recovery using IGM tomography. The properties of the protoclusters are discussed in Section 3, while Section 4 describes the algorithm we use to make maps from our mock observations. In Section 5, we describe a simple method for identifying protocluster candidates in the reconstructed maps. In Section 6, we synthesize mock surveys from our simulation, and test how protocluster identification depends on survey parameters. Finally, we provide a summary of our findings in Section 7.

2. SIMULATIONS

In order to validate our protocluster search strategy, and to study the purity and completeness of the sample we obtain, we make use of cosmological N-body simulations. We require a simulation which simultaneously covers a large cosmological volume (to have a statistically fair sample of the rare clusters and protocluster regions) while having a sufficiently small inter-particle spacing to model transmission in the IGM. The requirements are sufficiently demanding that we have used a pure N-body simulation, augmented with the fluctuating Gunn-Peterson approximation (FGPA; Petitjean et al. 1995; Croft et al. 1998; Meiksin & White 2001; Meiksin 2009). This simulation was also used in Lee et al. (2014c).

2.1. N-body simulation

Our simulation employed 2560^3 equal mass ($8.6 \times 10^7\,h^{-1}M_\odot$) particles in a $256\,h^{-1}$Mpc periodic, cubical box leading to a mean inter-particle spacing of $100\,h^{-1}$kpc. This is sufficient to model the large-scale features in the IGM at $z \simeq 2$ – 3 using the FGPA (Meiksin & White 2001; Rorai et al. 2013) and more than sufficient to find clusters at $z = 0$. The assumed cosmology was of the flat ΛCDM family, with $\Omega_m \simeq 0.31$, $\Omega_b h^2 \simeq 0.022$, $h = 0.6777$, $n_s = 0.9611$, and $\sigma_8 = 0.83$, in agreement with Planck Collaboration et al. (2013a). The initial conditions were generated using second- order Lagrangian perturbation theory at $z_{ic} = 150$, when the rms particle displacement was 40 per cent of the mean inter-particle spacing. The particle positions and velocities were advanced to $z = 0$, using a TreePM code (White 2002) assuming a spline-softened force with a Plummer equivalent smoothing length of $3\,h^{-1}$kpc. This TreePM code has been compared to a number of other codes and shown to perform well for such simulations (Heitmann et al. 2008).

2.2. Halo catalogs

At $z = 0$ and $z = 2.5$, we generated halo catalogs using a friends-of-friends (FoF; Davis et al. 1985) algorithm with a linking length $b = 0.168$. This algorithm partitions particles into groups bounded approximately by isodensity contours of roughly 100 times the mean density (e.g. Lacey & Cole 1994; White 2001, and references therein). Since we focus only on the most massive objects in our simulations, FoF halos are sufficient — more sophisticated halo finding methods will recover more detailed halo and subhalo properties, but with increased complexity and computational cost[1].

---

[1] For a recent review and comparison of halo finding methods see Knebe et al. (2011).

2.3. *Lyα flux field*

For the output at $z = 2.5$, we also generated mock Lyα forest spectra on a 2560^3 grid with the FGPA. This approximation makes use of the fact that adiabatic cooling of the gas in the presence of a photoionizing ultraviolet background leads to a tight density-temperature relation in the low density gas responsible for the Lyα forest seen in absorption against bright objects (Gnedin & Hui 1998; Meiksin 2009). The approximation has been shown to match more detailed hydrodynamical computations at the ten percent level (Meiksin & White 2001; Viel et al. 2002; McDonald 2003; Viel et al. 2006), and is certainly sufficient for our purposes.

The dark matter particle positions and velocities were deposited onto the grid using CIC interpolation (Hockney & Eastwood 1988). We then Gaussian filtered the density and velocity on the grid in order to approximate the pressure smoothing which affects the gas density. We assumed an IGM temperature at mean density $T_0 = 2 \times 10^4$ K, which gives a filtering scale of about $100 \, h^{-1}$kpc at the redshifts of interest here (e.g. Gnedin & Hui 1998; Viel et al. 2002; White et al. 2010; Rorai et al. 2013). Our results are largely insensitive to the details of this pressure smoothing procedure, since we are probing fluctuations on much larger scales (Mpc). We set the temperature according to the density-temperature relation $T = T_0(\rho/\bar{\rho})^{\gamma-1}$, with a standard choice for the equation of state parameter $\gamma = 1.6$ (Lee et al. 2014b). We compute the optical depth to HI Lyα scattering τ and the transmitted flux $F = e^{-\tau}$ assuming the HI density is proportional to the ratio of the recombination and photoionization rates $n_{\mathrm{HI}} \propto \rho^2 T^{-0.7} \Gamma^{-1}$ and that the line profile is a Doppler profile, and we normalize the optical depth such that the mean flux $\langle F \rangle = 0.8$, matching the recent observational result in Becker et al. (2013) for this redshift. This scheme ignores several phenomena that could affect the Lyα forest including spatial fluctuations in the temperature of the IGM due to reionization inhomogeneities, spatial fluctuations in the ultraviolet background due to the shot noise of sources, and galactic outflows. Fortunately, at the Mpc scale, the effects of galactic outflows and temperature fluctuations on flux should be rather small, while we expect the ultraviolet background to fluctuate on scales of several hundred Mpc (McDonald et al. 2005; Greig et al. 2014; Pontzen 2014; Gontcho et al. 2014). In the remainder of the paper, when we refer to flux, we mean the Lyα forest transmitted flux fraction perturbation $\delta_F = F/\langle F \rangle - 1$.

The final products we use from the simulation, then, are the halo catalogs at $z = 0$ and 2.5, including the positions of the particles within those halos at $z = 2.5$, and 3D grids of density and flux. We begin by studying the relationship between this ideal flux field and the halos and protoclusters. In Section 6, we will look at the impact of finite sightline density, resolution and noise on the recovery of the flux field.

3. PROTOCLUSTERS IN DENSITY AND LYα FOREST FLUX

The boundary between a rich group and a cluster is somewhat arbitrary, but we shall define a cluster at $z = 0$ as a halo with a FoF mass larger than $10^{14} \, h^{-1} M_\odot$. We have 425 halos above this mass in the simulation at $z = 0$ and these will form our sample. A protocluster is the
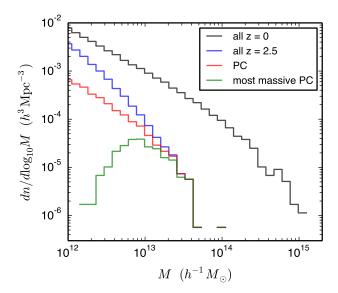

FIG. 1.— The halo mass functions for all halos at $z = 0$ (black), all halos at $z = 2.5$ (blue), protocluster halos (red), and the most massive halos in each protocluster (green). The massive end of the high redshift mass function is dominated by protocluster halos. The most massive halo in a protocluster is typically $10^{13} \, h^{-1} M_\odot$ at this redshift.

high-redshift progenitor of such massive halos, but due to the hierarchical process by which halos form, there is some ambiguity as to what constitutes the progenitor. At $z \simeq 2 - 3$, the mass which will eventually lie within the $z = 0$ halo is spread among several relatively large progenitor halos and in the nearby IGM, spread over tens of (comoving) Mpc. We tracked the cluster progenitor halos by finding all halos at $z = 2.5$ that contributed half or more of their mass to the resulting cluster. We show the mass functions of all $z = 2.5$ halos, of protocluster halos, and of the most massive halo in each protocluster in Figure 1. The high-mass end of the mass function is dominated by the halos that form clusters, but the protocluster halos do not make up all of the high mass halos. Protocluster halos only make up about half of the halos near $10^{13} \, h^{-1} M_\odot$ for instance. We found that the most massive progenitor halo is typically about $10^{13} \, h^{-1} M_\odot$, with more massive clusters having more massive progenitor halos on average. Only the most massive such halos are likely to host a hot, X-ray emitting ICM or be found as significant overdensities of galaxies. We also computed the second moment of the progenitor halo positions $\sqrt{[\sum_i m_i(\mathbf{x}_i - \bar{\mathbf{x}})^2]/[\sum_i m_i]}$, where $\bar{\mathbf{x}}$ is the average position and m_i and $\mathbf{x}_i$ are the halo masses and centers, as done in Chiang et al. (2013) to confirm the extent of the halos they found at this redshift. We found that the progenitor halos are spread over $4 - 8 \, h^{-1}$Mpc, in good agreement with their values at $z = 2 - 3$. However, in contrast to Chiang et al. (2013), we are interested less in the progenitor halos and more in the large-scale overdense region from which the mass of the cluster will be assembled.

In order to define the protocluster center, we tracked particles that form the core of the $z = 0$ cluster back to $z = 2.5$, and computed their center of mass (COM). The choice of particles that constitute the 'core' of the cluster is arbitrary, but the exact choice of particles does not

$\log_{10} \rho/\bar{\rho} \ (z=0)$

-0.4   0.0   0.4   0.8   1.2

$\log_{10} \rho/\bar{\rho} \ (z=2.5)$

-0.4   0.0   0.4   0.8   1.2

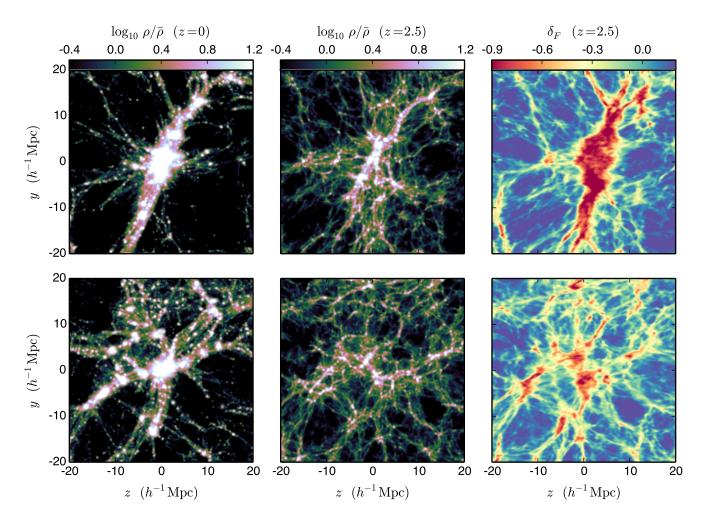$\delta_F \ (z=2.5)$

-0.9   -0.6   -0.3   0.0

FIG. 2.— Slices through the density and flux fields centered on two protoclusters. The line-of-sight direction is horizontal. The upper row shows a cluster/protocluster which is easily found by our method, while the lower row shows a more problematic case. The upper row cluster has a mass $M = 9 \times 10^{14} \, h^{-1} M_\odot$, while the lower row cluster has a mass $M = 3 \times 10^{14} \, h^{-1} M_\odot$. We chose these sample protoclusters based on the δ_F value at the protocluster center of mass (COM), where the top protocluster has the smallest δ_F value, and the bottom protocluster has the largest. The slices are $40 \times 40 \, h^{-1}$Mpc on a side and $5 \, h^{-1}$Mpc thick. In each row, the color scale shows the log overdensity or flux perturbation: (Left) the $z = 0$ density (centered on the cluster COM), (Middle) the $z = 2.5$ density (centered on the protocluster COM), (Right) the $z = 2.5$ flux perturbation, δ_F. Note that overdense regions correspond to regions of increased absorption, or more negative δ_F, and that correlation is quite strong on these scales. The small differences in the $z = 2.5$ density and flux fields are due to the density is shown in real-space while the flux is in redshift-space.

matter as long as the resulting COM does not change significantly. We chose to select the particles within $200 \, h^{-1}$kpc from the most bound (densest) cluster particle at $z = 0$. We refer to this collection of particles that makes up the cluster core as the N-densest particles. We found that changing the cutoff radius from 100 to $500 \, h^{-1}$kpc results in small changes to the protocluster center, on the level of $100 \, h^{-1}$kpc, which is negligible for objects spanning several Mpc. Inspired by Chiang et al. (2013), we define the protocluster radius $r_{\rm pc}$ as the radius of a sphere, centered on the protocluster center, enclosing 50 percent of the particles which belong to the halo at $z = 0$. We found the expected trend that more massive clusters have larger protocluster sizes. The $10^{\rm th}$ percentile radius is $3.3 \, h^{-1}$Mpc, the $50^{\rm th}$ percentile is $4.1 \, h^{-1}$Mpc, and the $90^{\rm th}$ percentile is $5.4 \, h^{-1}$Mpc. The largest half-mass radius we found in the simulation is $8.9 \, h^{-1}$Mpc, and this protocluster forms a $10^{15} \, h^{-1} M_\odot$ cluster. This, in combination with the moment of the

progenitor halo positions, gives us good reason to believe that protoclusters will stand out on scales of $\sim 4 \, h^{-1}$Mpc at this redshift.

We show two examples of protoclusters, as seen in density and Lyα forest flux, in Figure 2. The upper row shows a protocluster with a large coherent structure which will be easily found by our method, while the lower row shows a case where the protocluster is spread out and will prove much more difficult to find. The upper row cluster has a mass $M = 9 \times 10^{14} \, h^{-1} M_\odot$, while the lower row cluster has a mass $M = 3 \times 10^{14} \, h^{-1} M_\odot$. From left to right, we show the $z = 0$ density, $z = 2.5$ density, and the flux in a slice $40 \, h^{-1}$Mpc across and $5 \, h^{-1}$Mpc thick. Due to the physics of the IGM, the flux is tightly correlated with the matter density on large scales, with overdense regions leading to more absorption (low flux). In the protocluster in the upper row, the progenitor halos that merge to form the cluster can be easily seen in the middle column and lead to a large, coherent flux

decrement in the right column. The flux decrement in the lower row is still visible, but it is not as pronounced, because the halos making up the protocluster are more diffuse. We compared the progenitor halos of these clusters and found that at fixed mass, the protocluster in the upper row has three times as many halos and that the most massive halo is twice as massive, indicating that the upper row cluster forms earlier. The most massive progenitor halo in the upper row cluster has a mass of $3 \times 10^{13} \, h^{-1} M_\odot$ — a typical rich group mass — meaning that it should be easier to follow up at high redshift. Overall, we found that 40% of the protoclusters contain a halo with a mass $M > 10^{13} \, h^{-1} M_\odot$.

Not surprisingly, all of the protocluster regions lie on the high-density tail of the density distribution. We smoothed the density field with Gaussian filters of scales 2, 4, and $8 \, h^{-1}$Mpc (labeled ρ_2, ρ_4, and ρ_8 respectively) and compared the distributions of the full field and the protoclusters. We smooth the fields for two reasons: to mimic the characteristic resolution of our tomographic maps and because protoclusters should stand out most on scales of several Mpc. The top panel of Figure 3 shows the probability density function of the density $p(\rho)$ for random positions (solid) and for the protocluster regions (dashed). The majority of the protoclusters have densities exceeding the 95th percentile of the density distribution. This is clearer in the second panel showing the cumulative distribution $C(\rho)$, plotted as log-scaled $1 - C$ to highlight the high-density tail. Here, it is easy to see the 95th percentile density for the field, and compare to the protocluster distribution. Regardless of the smoothing scale, nearly all protoclusters have densities in the 95th percentile tail. In the bottom two panels, we show the probability density and cumulative distribution of the flux. Since the large-scale flux is so tightly correlated with the density, we find that the majority of protoclusters similarly lie in the low-flux tail of the distribution. Protoclusters can thus be found quite efficiently by searching for large-scale flux decrements (see also Cai et al. 2014). In 1D, large-scale flux decrements can also be created by damped Lyα systems (DLA) (Meiksin 2009). However, DLAs have physical extents of $< 100 \, h^{-1}$kpc, much smaller than our transverse scales, which make it very unlikely for DLAs to contaminate several nearby sightlines at the same redshift.

The radial profiles of the protocluster in density and flux are shown in Figure 4. These profiles were constructed by radially binning the $4 \, h^{-1}$Mpc smoothed fields, from the center of each protocluster (grey lines) and by stacking all protocluster profiles (black lines). Again, we use the smoothed fields to mimic the tomographic map resolution and to highlight protocluster scales. On the y-axis in both panels, we plot the standard-deviation normalized values (where we use the standard deviation of the smoothed field) to see how much protocluster profiles stand out relative to other fluctuations at this scale. The overdensity and flux decrement near the center is significant. We found that the profiles are even more pronounced in the $2 \, h^{-1}$Mpc smoothed fields, while in the $8 \, h^{-1}$Mpc smoothed fields, the profiles are shallow, and do not stand out significantly in the center. This indicates that smoothing at a scale of $8 \, h^{-1}$Mpc is likely too aggressive for our application.
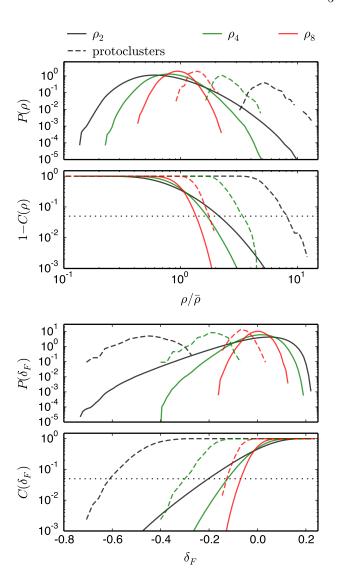

Fig. 3.— Distributions of the matter density and flux, smoothed with Gaussians of $\sigma = 2$, 4, and $8 \, h^{-1}$Mpc (labeled ρ_2, ρ_4, and ρ_8 with the broadest distributions having the smallest σ). Solid lines show the PDF for the entire volume while the dashed lines indicate the densities or fluxes at the protocluster positions. The top two panels show the matter density PDF, $P(\rho)$, and the cumulative distribution, $C(\rho)$, plotted as $1 - C$ to highlight regions of high density. The horizontal dotted black line shows the 95th percentile. We see that protoclusters preferentially lie in the highest density regions of the density field, smoothed on Mpc scales. The lower two panels show the PDF and cumulative distribution for the flux perturbation, δ_F. We see that protoclusters preferentially lie in the negative tails of the distribution.

We fit Gaussian profiles to the average density and flux profiles, and show the fits with dotted red lines. We also annotated the fit Gaussian σ values, which indicate that the protoclusters are overdense/under-fluxed over several Mpc. These results validate our strategy for finding protoclusters by looking for large-scale flux decrements in the Lyα forest.

In Figure 5, we show three protocluster properties vs. the resulting cluster mass $M(z = 0)$. We plot the individual protocluster values with light gray dots, and $M(z = 0)$ binned results (with std. dev. error bars) in
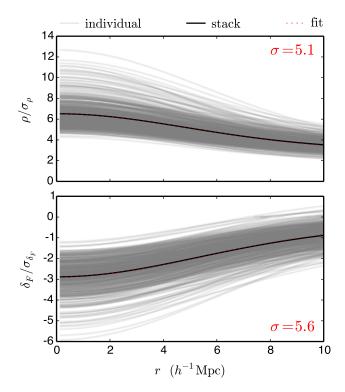
FIG. 4.— The radial density and flux profiles of the protocluster regions (from the $4\,h^{-1}$Mpc smoothed fields). We show the individual profiles in grey, the average profiles in black, and Gaussian fits in dotted red. (Top) the density profiles. We plot ρ/σ_ρ, where σ_ρ is the standard deviation of the field, since we are interested in how extreme the protocluster regions are. (Bottom) repeated with flux. The fit Gaussian scale σ is annotated in red.

FIG. 5.— Several protocluster properties vs. the resulting cluster mass $M(z=0)$. In each panel, we plot each protocluster as a gray dot, and the $M(z=0)$ binned result with std. dev. error bars in black. The red dashed lines show an approximate scaling. Top: the protocluster half-mass radius $r_{\rm pc}$. The red line is the $r \propto M^{1/3}$ relation, which fits well. Middle: the flux decrement $\delta_F/\sigma_{\delta_F}$, evaluated at the protocluster center, smoothed with a 4 h^{-1}Mpc Gaussian. We show $\delta_F/\sigma_{\delta_F}$ on the y-axis to show how extreme the protocluster regions are. The protoclusters that stand out the most form the most massive clusters. The red line is an empirical fit of $\delta_F \propto -2.9 \log M(z=0)$. Bottom: the mass of the most massive halo in the protocluster. The red line assumes linear growth, $M(z=0) \propto M(z=2.5)$. The high mass clusters appear to grow faster than the linear scaling, although this could be due to small numbers.

black. The red dashed lines show approximate scalings for each quantity. The top panel shows the protocluster half-mass radii, which scales with the cluster mass. We expect the half-mass and virial radii to scale similarly with mass. The red line shows the $r \propto M^{1/3}$ relation, which fits the protocluster sizes well. This falls in line with the expectation that more massive clusters form from larger overdense regions. The second panel shows the protocluster flux decrement $\delta_F/\sigma_{\delta_F}$, evaluated at the protocluster centers from the $4\,h^{-1}$Mpc smoothed flux field. In this case, the red line is entirely empirical. We noticed that the flux decrement scales roughly linearly with $\log M(z=0)$ and found a good fit using $\delta_F \propto -2.9 \log M(z=0)$. This means that more massive clusters stand out more significantly in the flux field, although the flux decrement from low mass clusters is not very significant. Some low mass clusters have decrements of only 1 or 2 σ, which are probably too difficult to distinguish from other background fluctuations. Clusters with a mass greater than $3 \times 10^{14}\,h^{-1}M_\odot$, however, mostly originate in regions that are greater than 3σ flux decrements. For this reason, we expect to focus on finding more massive protoclusters. Finally, in the bottom panel, we show the mass of the most massive protocluster halo. The red line shows the linear scaling $M(z=0) \propto M(z=2.5)$, although the cluster masses appear to grow a bit faster than this. Although there is significant scatter in this relationship, this confirms that more massive progenitor halos form the more massive
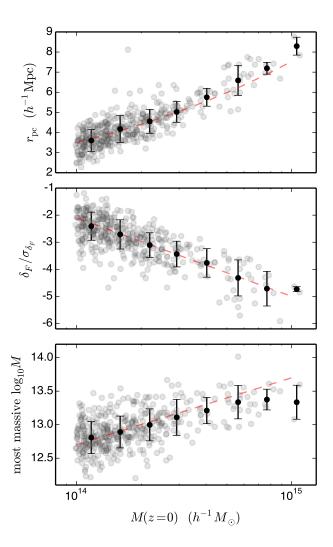
clusters. This is similar to what Conroy et al. (2008) found, where halos roughly maintain mass rank order as they evolve from $z=2$ to $z=0$. Altogether, these trends suggest that finding progenitors of the most massive clusters will be easiest, because they host the most massive halos, their flux decrement is more significant, and because the decrement covers a larger volume. We check if this expectation holds up in Section 6.

This section contains a basic characterization of protocluster environments, but it is important to note that our protoclusters have a wide range of sizes, profiles and overdensities (see also Chiang et al. 2013). We have presented a simplified view of protoclusters focused on prop-

erties that will allow us to identify them in flux maps. The full picture of these environments is probably much more complex, as illustrated by the examples in Figure 2. Large statistical samples are required to obtain a representative view of protocluster formation and the impact of the protocluster environment on galaxy formation and evolution.

4. RECONSTRUCTION METHOD

We have argued that an efficient method for finding protoclusters is to look for large-scale decrements in the flux field. In this section we discuss how to make intermediate-resolution maps of the flux field, suitable for protocluster searches, from observations of closely-separated sightlines.

We use a Wiener filter (Wiener 1949; Press et al. 1992) to estimate the 3D flux field from the noisy observations along multiple sightlines, as advocated by Caucci et al. (2008); Lee et al. (2014a). The Wiener filter provides the minimum variance, unbiased linear estimator of the field (under the assumption of a normal distribution) and can be used to interpolate the data into regions which are not directly sampled, making it ideal for our purposes[2]. We briefly review the derivation of the Wiener filter, as we use it, in Appendix A.1, where we also describe our efficient numerical implementation. Collecting all of the observations of normalized flux into a data vector, $\mathbf{d}$, which is the sum of a signal and noise $\mathbf{d} = \mathbf{s} + \mathbf{n}$, the Wiener filter estimate of the signal at an arbitrary position is $\hat{\mathbf{s}} = \mathbf{L}\mathbf{d}$ with $\mathbf{L} = \mathbf{S}_{mp}(\mathbf{S}_{pp} + \mathbf{N})^{-1}$. Here $\mathbf{S}$ is the assumed signal covariance, where m and p indicate map or pixel coordinates, and $\mathbf{N}$ is the noise covariance. The reconstructed map is thus

$$\hat{\mathbf{s}} = \mathbf{S}_{mp}(\mathbf{S}_{pp} + \mathbf{N})^{-1}\mathbf{d} \tag{1}$$

Following Caucci et al. (2008), we model $\mathbf{S}$ as the product of two Gaussians for separations along and transverse to the line-of-sight:

$$S_{ij} = \sigma_F^2 \exp\left[-\frac{(\mathbf{x}_{\perp,i} - \mathbf{x}_{\perp,j})^2}{2l_\perp^2} - \frac{(x_{\parallel,i} - x_{\parallel,j})^2}{2l_\parallel^2}\right] \tag{2}$$

For the noise covariance, we assume that the pixel-to-pixel noise is independent, so that $N_{ij} = n_i^2 \delta_{ij}$. These assumptions are approximations, but they are reasonably accurate in the context of the Lyα forest and the reconstruction is not sensitive to the form assumed (see tests in Appendix A.2). Assuming this form for the signal covariance and that the noise covariance is diagonal provides a huge advantage computational advantage, as it allows us to never store the matrices directly and instead compute them as needed. This reduces the space complexity of the algorithm from N^2 to N so that we can still fit large problems on a single node. We provide more details of our implementation in Appendix A.3.

In this work, we only discuss reconstructing the flux field since it is sufficient for our application of finding protoclusters. However, we note here that other authors have considered schemes to reconstruct the matter density in the context of galaxies as tomographic tracers (Willick 2000; Kitaura et al. 2009; Courtois et al. 2012)

---

[2] See Pichon et al. (2001) for a more general method than Wiener filtering and Cisewski et al. (2014) for a non-parametric method

and the Lyα forest (Kitaura et al. 2012) and how to account for redshift-space distortions in the reconstruction.

5. PROTOCLUSTER IDENTIFICATION

As shown in Section 3, protoclusters are significant outliers in density and flux on scales of several Mpc. In this section, we show how we can exploit this fact to identify protoclusters in the flux maps.

There are many ways we could test for large-scale outliers, but we start with a simple process of smoothing with a preferred scale and applying a threshold. We smooth the flux field with a 3D Gaussian filter, typically with a scale $\sigma = 4\,h^{-1}$Mpc. Since the protocluster profiles are roughly Gaussian with a similar scale, this acts much like a matched filter. We tried running this procedure with the different σ values of 2, 4, and $8\,h^{-1}$Mpc and found that the $4\,h^{-1}$Mpc version performs best. Next, we select all points below some threshold, and group nearby points together. The grouping process is also simple, where we merge points within $4\,h^{-1}$Mpc. This merging process ensures that we do not mistakenly break up low-flux regions and also that each region has a buffer from other regions. Finally, for each group of points, we define a protocluster candidate as a $4\,h^{-1}$Mpc sphere centered on the minimum flux point in the group. In principle, we could adjust the choices of the smoothing scale, merging distance, and candidate radius independently to optimize the candidate selection, but we found it was not necessary for our purposes, where this simple procedure already performs well. For a more advanced identification method, see the optimal filter presented in Appendix B.

To get an idea of how this identification procedure performs, we first tested identifying protocluster candidates from an ideal flux field. We took the high-resolution flux field from the simulation, smoothed with a $4\,h^{-1}$Mpc Gaussian, and downsampled to a typical map resolution (grid spacing) of $1\,h^{-1}$Mpc. We chose a threshold of -3.5 times the standard deviation of the field, because we found this value performed best for finding protoclusters forming $> 3 \times 10^{14}\,h^{-1}M_\odot$ clusters (see Figure 5). When we used more negative threshold values, we only found the most massive protoclusters, and when we used more positive threshold values, the protocluster purity decreased and very large protoclusters were mistakenly merged. These threshold points make up about 10^{-3} of the simulation volume, and were grouped into 68 candidates.

For each candidate, we computed the number of halos in the $4\,h^{-1}$Mpc radius sphere and found the maximum mass halo within the sphere. We assigned each maximum mass halo to a $z = 0$ halo by tracking its particles to $z = 0$ and checking which $z = 0$ halo contained the most of its particles. The candidate is a protocluster if this $z = 0$ halo mass is $> 10^{14}\,h^{-1}M_\odot$. We also computed these basic halo statistics for randomly positioned spheres to compare to a field distribution. The results are shown in Figure 6, where we plot the candidate number of halos, maximum $z = 2.5$ halo mass, and resulting $z = 0$ halo mass vs. the candidate $\delta_F/\sigma_{\delta_F}$ value. These panels clearly show that the low-flux selected candidates have large halo overdensities and are almost all protoclusters. In the top panel, we plot the number of halos in the protocluster candidate regions which shows that the can-
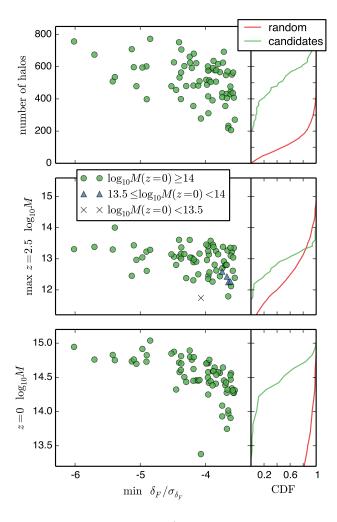
FIG. 6.— Halo statistics in $4\,h^{-1}$Mpc spheres centered on protocluster candidates (selected by flux decrement) compared to centered on random points. In each row, we plot the candidates as points on the left and on the right, we plot the cumulative distribution of the candidates and random points. Top: The number of halos in the sphere. Middle: The mass of the maximum mass halo, where the marker indicates the candidate category based on the $z = 0$ mass (green dots for clusters, blue triangles for rich groups, and black crosses for anything smaller). Bottom: The $z = 0$ mass of the maximum mass halo.

many galaxies and massive galaxies that can be followed up.

The candidate and random sphere cumulative distributions for the maximum $z = 2.5$ mass halos are particularly interesting. Half of the candidate maximum mass halos are in the mass range of $10^{12} - 10^{13}\,h^{-1}M_\odot$ and the remaining half are in the $10^{13} - 10^{14}\,h^{-1}M_\odot$ range. In the random distribution, half of the maximum mass halos are $< 10^{12}\,h^{-1}M_\odot$, but there is a significant tail to high masses and the distributions cross at $3 \times 10^{13}\,h^{-1}M_\odot$. We checked the total population of $3 \times 10^{12}\,h^{-1}M_\odot$ halos at $z = 2.5$ and found that only 30% end up in clusters by $z = 0$. This suggests that our identification procedure is not just picking out the most massive halos, but finds massive halos with the right environments to form clusters. This is supported by the cumulative distributions in the bottom panel, where the candidate and random position distributions are well-separated again. Despite our simple identification procedure, these results demonstrate that searching flux maps for large flux decrements is very effective for finding protoclusters.

We used a fairly conservative threshold value ($-3.5\sigma_{\delta_F}$) in order to achieve a high candidate sample purity of 93%, compared to the random sample purity of 5%. However, this comes with the cost of missing many of the low-mass protoclusters. We checked the candidate completeness vs. cluster mass, and found that above $3.5 \times 10^{14}\,h^{-1}M_\odot$, the completeness is constant and around 80%. Below this mass, the completeness falls off, reaching 50% around $2.4 \times 10^{14}\,h^{-1}M_\odot$, and 25% around $1.5 \times 10^{14}\,h^{-1}M_\odot$. As shown in Figure 5, we expect only more massive protoclusters (those forming $> 3 \times 10^{14}\,h^{-1}M_\odot$ clusters) to stand out significantly in the flux maps, using a simple threshold at least. At the same time, the number of clusters quickly increases as we lower the mass, since these objects are on the tail of the mass function. This unfortunate combination drives our sample completeness to very small numbers for protoclusters forming low-mass clusters. However, for moderate-mass protoclusters (forming $> 3 \times 10^{14}\,h^{-1}M_\odot$ clusters), the method performs well and successfully identifies $70 - 80\%$ of the population.

6. MOCK SURVEYS

In this section, we construct several tomographic mock surveys and run reconstructions on the synthetic data to test how our protocluster identification will perform on realistic data. Specifically, we are interested in what we can achieve with different values of the average sightline separation $\langle d_\perp \rangle$, as Lee et al. (2014a) demonstrated that this is the most important factor in determining the quality (effective SNR) in the reconstructed maps. Lee et al. (2014a) provides a simple relation between the exposure time $t_{\exp}$, the minimum signal-to-noise ratio (SNR) per Å $SNR_{\min}$, and the average sightline separation: $t_{\exp} \propto SNR_{\min}^{2}\langle d_\perp \rangle^{-1.6}$. We assume a fixed $SNR_{\min}$ of 1.5, similar to the recent observations of Lee et al. (2014c), so that the exposure time is just a proxy for the desired average sightline separation. In principle, we could vary the sightline density and the SNR independently, but in practice this is not a useful test. If we increase the exposure time to build up the SNR, it is more advantageous (in terms of the reconstruction qual-

didates are all fairly rich environments. The candidate regions are on average 5 times the field median value and the cumulative distributions are well-separated. We note that our minimum halo mass is about $4 \times 10^{9}\,h^{-1}M_\odot$, corresponding to the requirement that an FoF halo contains at least 50 particles. The middle panel shows the candidates' maximum-mass halo masses, with markers indicating the candidate category based on the $z = 0$ mass. The green circles are clusters, the blue triangles are nearly clusters, and the black cross is a failure. We also plot the $z = 0$ halo masses in the bottom panel. The four "nearly" protocluster candidates have $z = 0$ masses of 5.6, 8.1, 8.5, and $9.4 \times 10^{13}\,h^{-1}M_\odot$, while the failure candidate has a $z = 0$ mass of $2.4 \times 10^{13}\,h^{-1}M_\odot$. In all panels, we see the expected trend that the more significant candidates (in terms of the minimum flux value) have richer environments and result in more massive clusters. This also illustrates how the identified protoclusters are more than overdense regions — they already host

ity) to target fainter sources and increase the sightline density. We initially chose values of $\langle d_\perp \rangle = 2, 2.5, 3, 4,$ and $6\,h^{-1}\mathrm{Mpc}$. We expect that a resolution of $2\,h^{-1}\mathrm{Mpc}$ will be difficult but possible with existing instruments, while a spacing of $4\,h^{-1}\mathrm{Mpc}$ is fairly coarse, and we expected $6\,h^{-1}\mathrm{Mpc}$ to perform poorly for our application. We note that the sightlines in Lee et al. (2014c) have an average separation of $2.3\,h^{-1}\mathrm{Mpc}$. When we found that the $\langle d_\perp \rangle = 6\,h^{-1}\mathrm{Mpc}$ separation run still performed decently, we added a survey configuration meant to mimic the Baryon Oscillation Spectroscopic Survey (BOSS) survey (Dawson et al. 2013). For the BOSS-like configuration, we chose an average sightline separation of $15\,h^{-1}\mathrm{Mpc}$, which is roughly the spacing for the $200\,\mathrm{deg}^2$ of the survey with a source density of $1.5 - 2$ times the mean.

We construct mock surveys using our full $(256\,h^{-1}\mathrm{Mpc})^3$ box. We first choose skewer positions by drawing random (x, y) coordinates in the box. We take the ideal F values along the skewer, smooth the signal based on a typical instrumental resolution $R = 1100$, and bin in pixel widths of $1.2\,\text{Å}$. We call this smoothed and binned flux F_{inst}. For each spectrum, we choose a constant per pixel SNR. We draw a random SNR value from a simple SNR distribution described below. Next, we realize noise for each spectrum based on its per pixel SNR value. For each pixel, we draw a random noise value from a normal distribution with scale $\sigma = \langle F \rangle / \mathrm{SNR}$. We add the noise vector F_{noise} to F_{inst} to get the final mock fluxes F_{syn}. Altogether, the input to the reconstruction includes the pixel positions $\mathbf{x}$, the data vector $\mathbf{d} = \mathbf{F}_{\mathrm{syn}}/\langle F \rangle - 1$, and the noise vector $\mathbf{n} = \mathbf{1}/\mathrm{SNR}$.

We model the sightline SNR distribution as a power law, with a scaling based on the LBG luminosity function and the observed distribution in Lee et al. (2014c). We define the number of sightlines per deg^2 as $n_{\mathrm{los}} = (70\,h^{-1}\mathrm{Mpc}/\langle d_\perp \rangle)^2\,\mathrm{deg}^{-2}$ for our cosmology and $z = 2.5$. Our model is $dn_{\mathrm{los}}/d\mathrm{SNR} \propto \mathrm{SNR}^{-\alpha}$, and we want to determine values of α. Based on fits to the LBG luminosity function, Lee et al. (2014a) found that $d\log n_{\mathrm{los}}/dg$ is close to unity for the sources we are interested in, where g is the source g-band magnitude. Combined with the relation $d\log\mathrm{SNR}/dg = -2.5$, we have $\alpha = -d\log n_{\mathrm{los}}/d\log\mathrm{SNR} = 2.5$. This is a good approximation, but as we probe brighter in the luminosity function and sit more on the exponential tail, we know that $|d\log n_{\mathrm{los}}/dg|$ must increase. To correct for this, we take the SNR distribution from our pilot observations, rescale them based on $\mathrm{SNR}_{\mathrm{new}}/\mathrm{SNR}_{\mathrm{obs}} = (\langle d_\perp \rangle_{\mathrm{new}}/\langle d_\perp \rangle_{\mathrm{obs}})^{-0.8}$, and fit a power law. For our choices of $\langle d_\perp \rangle = 2, 2.5, 3,$ and $4\,h^{-1}\mathrm{Mpc}$, we found $\alpha = 2.7, 2.9, 3.5, 3.6$. For larger separations, we did not have enough bright sources in the pilot observations to reliably estimate α, so we kept $\alpha = 3.6$. We note that for large separations, we would also target more QSOs, which have a smaller $|d\log n_{\mathrm{los}}/dg|$ value at these magnitudes, and provides a natural maximum value for α.

Altogether, we ran 30 mock surveys and reconstructions. For each choice of $\langle d_\perp \rangle$, we ran 5 reconstructions to check how the results varied with a fixed ideal δ_F, but different skewer sampling and noise realizations. For

TABLE 1
PROTOCLUSTER CANDIDATES AND SUCCESS RATES

Map	t_{exp} (hrs)	N_{cand}	f_{PC}	f_{NPC}	f_{fail}
ideal	N/A	68	0.93	0.06	0.01
random spheres	N/A	1000	0.05	0.07	0.88
$\langle d_\perp \rangle = 2\,h^{-1}\mathrm{Mpc}$	2.7	73	0.89	0.08	0.03
$\langle d_\perp \rangle = 2.5\,h^{-1}\mathrm{Mpc}$	1.9	68	0.89	0.09	0.01
$\langle d_\perp \rangle = 3\,h^{-1}\mathrm{Mpc}$	1.4	76	0.84	0.10	0.06
$\langle d_\perp \rangle = 4\,h^{-1}\mathrm{Mpc}$	0.90	77	0.78	0.15	0.07
$\langle d_\perp \rangle = 6\,h^{-1}\mathrm{Mpc}$	0.47	72	0.61	0.20	0.20
$\langle d_\perp \rangle = 15\,h^{-1}\mathrm{Mpc}$	N/A	26	0.35	0.10	0.55

Protocluster identification success rates for the ideal δ_F field and randomly-positioned spheres compared to the mock survey reconstructions. t_{exp} is the corresponding exposure time to achieve the desired sightline spacing (rescaled from the Keck/LRIS setup in Lee et al. (2014c)). N_{cand} is the number of candidates found in the map and the f values are the fractions of candidates broken into three class: protoclusters (PC), nearly protoclusters (NPC), and failures (fail). The numbers reported for the mock reconstructions are averages over the 5 realizations of sightline positions and noise. The $\langle d_\perp \rangle = 15\,h^{-1}\mathrm{Mpc}$ configuration is meant to reproduce the relatively high sightline density areas of the BOSS survey.

all reconstructions, we fixed $\sigma_F^2 = 0.05$, $l_\parallel = 2\,h^{-1}\mathrm{Mpc}$, and $l_\perp = \langle d_\perp \rangle$ as done in Lee et al. (2014a). The small-separation runs were much more time consuming than the large-separation runs since the $N_{\mathrm{pix}} \propto \langle d_\perp \rangle^{-2}$ and the algorithm scales with N_{pix}^2, so that a run with a half the average sightline separation takes 16 times longer.

We tested the success of the surveys by running the protocluster identification procedure on the mock maps and comparing to the halo catalog, just as we did for the ideal field in the previous section. Again, we used a smoothing scale of $4\,h^{-1}\mathrm{Mpc}$, a threshold of -3.5 times the standard deviation, and a region size of $4\,h^{-1}\mathrm{Mpc}$. Overall, we found an good agreement between protocluster candidates in the ideal and reconstructed fields, and that the success rates decrease with increasing average sightline spacing, as expected. In Table 1, we list the number of candidates identified in each map, and the fraction of candidates that fell into classes of protoclusters (PC), nearly protoclusters (NPC), and failures (fail). These classes follow the definitions used earlier in Figure 6, where protoclusters form clusters $(M \geq 10^{14}\,h^{-1}M_\odot)$, nearly protoclusters almost form clusters $(10^{13.5}\,h^{-1}M_\odot \leq M < 10^{14}\,h^{-1}M_\odot)$, and failures are anything less massive $(M < 10^{13.5}\,h^{-1}M_\odot)$. The mock results are averaged over the 5 survey realizations for each configuration. The number of candidates in the reconstructed maps is consistent with the result for the ideal field, although slightly higher, except for the BOSS-like survey which is much lower. If we scale the number of candidates $(N_{\mathrm{cand}} \sim 70)$ found in the simulation volume of $(256\,h^{-1}\mathrm{Mpc})^3$ to the final CLAMATO volume of $70 \times 70 \times 230\,(h^{-1}\mathrm{Mpc})^3$, we should find 5 candidates. However, using a smaller threshold will yield many more candidates, if the decrease in purity can be accommodated.

There is a clear trend of the success rates vs. the average sightline separation. As the sightline separation increases, the map quality decreases, and the sightlines begin to miss protocluster structures leading to the decline in success. Additionally, as the noise in the map
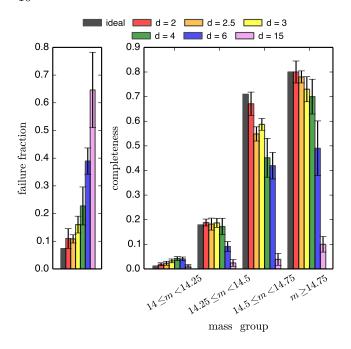
FIG. 7.— Candidate failure fractions and completeness identified in the ideal and mock maps. Left: Fraction of candidates that are failures ($M(z = 0) < 10^{14} h^{-1} M_\odot$). Right: Candidate completeness measured in 4 cluster mass bins, where the mass range in $m = \log_{10}[M/(h^{-1}M_\odot)]$ is indicated on the x-axis. The mock map counts are averages over 5 realizations, with std. dev. error bars. As the sightline separation increases, we see a steady increase in contamination, and the success fraction decreases. In the low-mass cluster bins, the mock survey completeness is sometimes higher than the noiseless map. This is a result of noise in the mock reconstructions pushing some less significant protoclusters over the chosen threshold value.

increases, the false positive rate increases. When we increase the sightline separation to larger than $10 h^{-1}\mathrm{Mpc}$, the quality of the map degrades significantly, which is reflected in the BOSS-like success rates and lower number of candidates. For small separations, the protocluster identification success rate is close to ideal — 93% in the ideal case and 89% for $\langle d_\perp \rangle = 2$ and $2.5 h^{-1}\mathrm{Mpc}$. Even with a coarse sightline separation of $4 h^{-1}\mathrm{Mpc}$, the success rate is 78%, and this only drops to 60% with the $6 h^{-1}\mathrm{Mpc}$ separation that we thought might be catastrophic.

In the BOSS-like separation surveys, the candidate purity is much lower. This is expected since the average spacing in this case is larger than all but the largest protoclusters. However, with random positions, it is possible for several sightlines to overlap with a protocluster and this configuration still performs significantly better than random. We believe the purity in the BOSS-like configuration could also be improved if we considered sightline positions, and only saved candidates with many overlapping sightlines.

In Figure 7, we show the candidate completeness and failure rates for the various survey configurations. On the left, we plot the fraction of candidates that did not form clusters. The mock map values are averages over the 5 realizations and we show the std. dev. error bars. We see a steady increase in the candidate contamination as the sightline separation increases. On the right, we plot the candidate completeness measured in four cluster

mass bins. For reference, the numbers of protoclusters from the full sample in these bins are 251, 123, 31, and 20. In the two high mass bins, the completeness of the $\langle d_\perp \rangle = 2$, 2.5, and $3 h^{-1}\mathrm{Mpc}$ surveys is similar to the ideal result. The completeness decreases for larger separations, although it is still about 50% for the $\langle d_\perp \rangle = 4$ and $6 h^{-1}\mathrm{Mpc}$, but only $5\% - 10\%$ for the BOSS-like survey. For the two low mass bin, the completeness overall is much lower, as discussed in the previous section. The completeness falls off for very large separations, as before, but for small separations, the completeness is sometimes larger than the ideal map. This is due to the noise in the reconstructions scattering some low mass protoclusters over the threshold value. That is, for some protoclusters that did not make the cut in the noiseless map, the reconstruction noise fortunately pushes them over the edge. Overall, this result makes us confident that we can find a large fraction of the protoclusters that form $> 3 \times 10^{14} h^{-1}M_\odot$ clusters with a CLAMATO-like survey.

In order to understand the cases where our protocluster identification method failed (either missing protoclusters or selecting false positives), we looked at many slices of individual candidates. We performed a union of all candidates identified in the ideal map and in the mock reconstructions, based on the candidate's $z = 0$ halo ID, and tracked which candidates were identified in which maps. After visually inspecting many candidates, we found that we could group the failures into four categories which we called dropout, bad merge, false positive, and borderline protocluster. We illustrate these cases with example candidates in Figure 8. Each row is a separate candidate, and the columns show the same slice from the ideal map and the $\langle d_\perp \rangle = 2$, 3, 4, and $6 h^{-1}\mathrm{Mpc}$ mock maps. If the candidate was identified in the map, we marked the center with a black cross. We also annotated the $\delta_F/\sigma_{\delta_F}$ value from each map (at the candidate center) under the image. In the top row, we show a successful case, where the candidate forms a massive cluster, and the protocluster is found in all of the maps. This case was not very common when we included the large $6 h^{-1}\mathrm{Mpc}$ separation maps, but it was usually the case for the most massive protoclusters that created a significant ($> 5\sigma$) flux decrement.

The first failure case, dropout, is the most common scenario for a missed protocluster identification. The protocluster creates a clear flux decrement in the ideal map and small separation survey maps, but the signal drops out in the large separation survey maps. An example is shown in the second row of Figure 8. In the example shown, the protocluster is successfully identified in the ideal and small $\langle d_\perp \rangle$ maps, but as the sightline separation increases, the region is less well-sampled and the flux values in the region never drop below the threshold. We also found plenty of cases where the candidate is missed in the $\langle d_\perp \rangle = 3$ or $4 h^{-1}\mathrm{Mpc}$ maps, but found again in the larger separation maps, just due to how the sightlines and the protocluster line up in a given random survey realization.

The second failure case, bad merge, is another scenario that results in missing a protocluster, and is due to a weakness in our method for merging points during the identification procedure. We found a few cases where
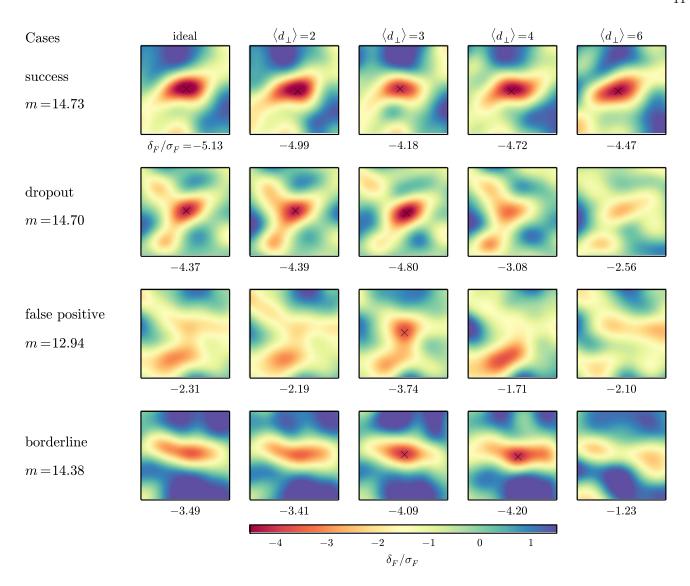
FIG. 8.— Slices from the ideal and mock maps centered on four candidates scenarios. The images show the $\delta_F/\sigma_{\delta_F}$ values in slices that are $40\,h^{-1}\mathrm{Mpc}$ across and $2\,h^{-1}\mathrm{Mpc}$ thick. From left to right, we show the ideal field and the mock reconstructions with increasing $\langle d_\perp \rangle$, and we mark successful identifications with a black cross. We also annotate the $\delta_F/\sigma_{\delta_F}$ value in the center of the map under each image. For each row, we annotate the case name and candidate mass $m = \log_{10}[M/(h^{-1}M_\odot)]$ on the left. Top row: A success case where the protocluster is identified in all maps. Second row: As the average sightline separation increases, the sightlines do not sample the low flux region well enough and the candidate "drops out". Third row: A moderately low flux region with additional noise can create a false positive. Bottom row: A borderline protocluster where the reconstruction noise scatters the candidate over the threshold value. There is another failure case (bad merge) not shown here, but explained in the text.

two protoclusters were linked by a dense filament, so that the two regions that should have been separate candidates were mistakenly merged. The grouped points were usually similar shapes in the different maps, but the flux minimum could end up in either protocluster depending on the reconstruction noise. If these candidates were correctly partitioned during the merging step, there would be another successful identification in each map.

In regions of moderately low flux, it is possible for the reconstruction noise to scatter low, and create false positives. This scenario is origin of the increasing contamination (failure fraction) with increasing sightline separation. The third row of Figure 8 shows an example of this, where the candidate is not a protocluster, but is mistakenly identified in one of the maps. Of course, sometimes

this reconstruction noise also scatters low mass protoclusters in the right direction. This is the origin of the final scenario we called borderline protoclusters. In this case, the protocluster creates a flux decrement just under the threshold, so that it is not identified in the noiseless map, but noise can scatter it over the threshold, so that it is identified in the mock reconstruction. An example is shown in the bottom row of Figure 8, where the flux decrement in the noiseless map is just under the threshold. In the $\langle d_\perp \rangle = 3$ and $4\,h^{-1}\mathrm{Mpc}$ reconstructions, the noise scatters the flux decrement to over 4σ, which makes it a successful candidate.

7. CONCLUSIONS

In this paper, we characterized the signature of protoclusters at $z \simeq 2 - 3$, and demonstrated the success

of a simple method for finding these protoclusters from the associated Lyα forest flux decrement. The tomographic reconstruction of the 3D Lyα forest transmitted flux field from individual sightlines is the crucial step to this method. In order to handle datasets with large numbers of pixels, we implemented a new fast Wiener Filter code, which we are making publicly available. This code will make it possible to run reconstructions on the scale of $N_{\rm pix} \gtrsim 10^6$, larger than the expected size of the ongoing CLAMATO survey.

We identified protoclusters at $z = 2.5$ using a large cosmological N-body simulation with sufficient resolution to capture individual absorption systems comprising the Lyα forest and covering enough volume to contain a respectable cluster sample. We constructed FoF halo catalogs for each simulation snapshot and defined clusters at $z = 0$ with a mass cut of $M \geq 10^{14}\,h^{-1}M_\odot$. We then identified protoclusters by tracking cluster member particles from $z = 0$ back to $z = 2.5$ (by particle ID) and characterized the protocluster regions. The key signature of protoclusters is that they are outliers in density and flux on large scales. We found that protocluster centers are above the $95^{\rm th}$ percentile of the density and flux decrement and that the half-mass radius of typical protoclusters at this redshift is $4\,h^{-1}$Mpc. The density and flux profiles of protocluster regions are well fit by a Gaussian with a scale of $5\,h^{-1}$Mpc, suggesting that maps with several Mpc resolution should easily resolve these structures. We also found that the flux decrement and radius of a protocluster increases with its $z = 0$ mass, so that it is easiest to find the protoclusters that form the more massive clusters.

We reviewed our tomographic reconstruction method (a Wiener Filter) and some specifics of our application. Specifically, we assume a certain form of the signal covariance and that the noise covariance is diagonal. These assumptions significantly reduce the space complexity of our algorithm, so that we can easily fit the calculations on a single node, avoiding significant communication costs and taking advantage of shared-memory parallelism. Additionally, this design will easily take advantage of upcoming compute architectures, where the number of cores per node is expected to increase in the near future, and could easily be extended to run on GPUs.

We designed a procedure to identify protocluster candidates in the flux maps. To choose candidates we smooth the map, apply a threshold, and group the remaining points into candidates. We ran the procedure on noise-less maps and compared to the simulation halo catalog, finding that we can achieve 90% candidate purity with this simple method. We also confirmed that the method tends to find protoclusters that form the most massive clusters ($> 3 \times 10^{14}\,h^{-1}M_\odot$). The most massive halos in the identified protoclusters have masses of about $10^{13}\,h^{-1}M_\odot$ — still very difficult to find at these redshifts using alternative methods.

Finally, we created realistic mock surveys (similar to the recent observations of Lee et al. (2014c)) and reconstructed the flux maps with our code. We found that surveys with an average sightline spacing $\langle d_\perp \rangle = 2.5\,h^{-1}$Mpc performs essentially the same as the ideal, noiseless map. Such surveys should identify protoclusters with a 90% success rate, and find 70 – 80% of the protoclusters that form clusters with masses $> 3 \times 10^{14}\,h^{-1}M_\odot$. Using the same conservative threshold, we would identify 5 protoclusters in the planned CLAMATO volume. However, the volume should contain about 30 protoclusters including those that form lower mass clusters.

Finding protoclusters at $z \simeq 2 - 3$ remains an observationally challenging problem. With relatively simple methods, we have demonstrated a promising new technique for finding protoclusters at these redshifts. As shown in Lee et al. (2014a) IGM tomography offers a novel method for mapping large volumes with high efficiency using existing facilities. The method can return large samples of protoclusters and does not suffer from projection effects (or redshift errors). The Lyα forest also has the advantage of only probing mildly nonlinear densities, allowing for *ab initio* calculation of the density-observable relation (i.e. the bias) via numerical simulations. Future work can easily extend this to reconstruct density maps, include redshift-space distortions, and incorporate more advanced models of protoclusters.

REFERENCES

Angulo, R. E., Springel, V., White, S. D. M., et al. 2012, MNRAS, 425, 2722

Baugh, C. M. 2006, Reports on Progress in Physics, 69, 3101

Becker, G. D., Hewett, P. C., Worseck, G., & Prochaska, J. X. 2013, MNRAS, 430, 2067

Benson, A. J. 2012, New Astronomy, 17, 175

Benson, A. J., & Bower, R. 2010, MNRAS, 405, 1573

Bleem, L. E., Stalder, B., Brodwin, M., et al. 2014, ArXiv e-prints, arXiv:1403.7186

Böhringer, H., Schuecker, P., Guzzo, L., et al. 2004, A&A, 425, 367

Burenin, R. A., Vikhlinin, A., Hornstrup, A., et al. 2007, ApJS, 172, 561

Cai, Z., Fan, X., Bian, F., et al. 2014, in American Astronomical Society Meeting Abstracts, Vol. 223, American Astronomical Society Meeting Abstracts #223, 358.21

Caucci, S., Colombi, S., Pichon, C., et al. 2008, MNRAS, 386, 211

Chiang, Y.-K., Overzier, R., & Gebhardt, K. 2013, ApJ, 779, 127

—. 2014, ApJ, 782, L3

Cisewski, J., Croft, R. A. C., Freeman, P. E., et al. 2014, MNRAS, 440, 2599

Conroy, C., Shapley, A. E., Tinker, J. L., Santos, M. R., & Lemson, G. 2008, ApJ, 679, 1192

Courtois, H. M., Hoffman, Y., Tully, R. B., & Gottlöber, S. 2012, ApJ, 744, 43

Croft, R. A. C., Weinberg, D. H., Katz, N., & Hernquist, L. 1998, ApJ, 495, 44

Cucciati, O., Zamorani, G., Lemaux, B. C., et al. 2014, A&A, 570, A16

Davis, M., Efstathiou, G., Frenk, C. S., & White, S. D. M. 1985, ApJ, 292, 371

Dawson, K. S., Schlegel, D. J., Ahn, C. P., et al. 2013, AJ, 145, 10

Diener, C., Lilly, S., Ledoux, C., et al. 2014, ArXiv e-prints, arXiv:1411.0649

Dolag, K., Borgani, S., Murante, G., & Springel, V. 2009, MNRAS, 399, 497

Ebeling, H., Edge, A. C., Allen, S. W., et al. 2000, MNRAS, 318, 333

Fabian, A. C. 1994, ARA&A, 32, 277

Feretti, L., Giovannini, G., Govoni, F., & Murgia, M. 2012, A&A Rev., 20, 54

Finley, H., Petitjean, P., Noterdaeme, P., & Pâris, I. 2014, ArXiv e-prints, arXiv:1408.4799

Finoguenov, A., Guzzo, L., Hasinger, G., et al. 2007, ApJS, 172, 182

Genel, S., Vogelsberger, M., Springel, V., et al. 2014, MNRAS, 445, 175

Gladders, M. D., & Yee, H. K. C. 2005, ApJS, 157, 1

Gnedin, N. Y., & Hui, L. 1998, MNRAS, 296, 44

Gontcho, S. G. A., Miralda-Escudé, J., & Busca, N. G. 2014, ArXiv e-prints, arXiv:1404.7425

Greig, B., Bolton, J. S., & Wyithe, J. S. B. 2014, ArXiv e-prints, arXiv:1411.1687

Haehnelt, M. G., & Tegmark, M. 1996, MNRAS, 279, 545

Hao, J., McKay, T. A., Koester, B. P., et al. 2010, ApJS, 191, 254

Heitmann, K., Lukić, Z., Fasel, P., et al. 2008, Computational Science and Discovery, 1, 015003

Hill, G. J., Gebhardt, K., Komatsu, E., & MacQueen, P. J. 2004, in American Institute of Physics Conference Series, Vol. 743, The New Cosmology: Conference on Strings and Cosmology, ed. R. E. Allen, D. V. Nanopoulos, & C. N. Pope, 224–233

Hockney, R. W., & Eastwood, J. W. 1988, Computer simulation using particles

Kitaura, F.-S., Gallerani, S., & Ferrara, A. 2012, MNRAS, 420, 61

Kitaura, F. S., Jasche, J., Li, C., et al. 2009, MNRAS, 400, 183

Knebe, A., Knollmann, S. R., Muldrew, S. I., et al. 2011, MNRAS, 415, 2293

Kochanek, C. S., White, M., Huchra, J., et al. 2003, ApJ, 585, 161

Koester, B. P., McKay, T. A., Annis, J., et al. 2007, ApJ, 660, 239

Kravtsov, A. V., & Borgani, S. 2012, ARA&A, 50, 353

Lacey, C., & Cole, S. 1994, MNRAS, 271, 676

Lee, K.-G., Hennawi, J. F., White, M., Croft, R. A. C., & Ozbek, M. 2014a, ApJ, 788, 49

Lee, K.-G., Hennawi, J. P., Spergel, D. N., et al. 2014b, ArXiv e-prints, arXiv:1405.1072

Lee, K.-G., Hennawi, J. F., Stark, C., et al. 2014c, ApJ, 795, L12

Marriage, T. A., Acquaviva, V., Ade, P. A. R., et al. 2011, ApJ, 737, 61

Martizzi, D., Jimmy, Romain, T., & Moore, B. 2014, MNRAS, 443, 1500

McCarthy, I. G., Schaye, J., Ponman, T. J., et al. 2010, MNRAS, 406, 822

McDonald, P. 2003, ApJ, 585, 34

McDonald, P., Seljak, U., Cen, R., Bode, P., & Ostriker, J. P. 2005, MNRAS, 360, 1471

Meiksin, A., & White, M. 2001, MNRAS, 324, 141

Meiksin, A. A. 2009, Reviews of Modern Physics, 81, 1405

Murphy, D. N. A., Geach, J. E., & Bower, R. G. 2012, MNRAS, 420, 1861

Muzzin, A., Wilson, G., Yee, H. K. C., et al. 2009, ApJ, 698, 1934

Peterson, J. R., & Fabian, A. C. 2006, Phys. Rep., 427, 1

Petitjean, P., Mueket, J. P., & Kates, R. E. 1995, A&A, 295, L9

Pichon, C., Vergely, J. L., Rollinde, E., Colombi, S., & Petitjean, P. 2001, MNRAS, 326, 597

Pierre, M., Pacaud, F., Duc, P.-A., et al. 2006, MNRAS, 372, 591

Planck Collaboration, Ade, P. A. R., Aghanim, N., et al. 2013a, ArXiv e-prints, arXiv:1303.5076

—. 2013b, ArXiv e-prints, arXiv:1303.5089

Pontzen, A. 2014, Phys. Rev. D, 89, 083010

Postman, M., Lubin, L. M., Gunn, J. E., et al. 1996, AJ, 111, 615

Press, W. H., Teukolsky, S. A., Vetterling, W. T., & Flannery, B. P. 1992, Numerical Recipes in C (2nd Ed.): The Art of Scientific Computing (New York, NY, USA: Cambridge University Press)

Reichardt, C. L., Stalder, B., Bleem, L. E., et al. 2013, ApJ, 763, 127

Rorai, A., Hennawi, J. F., & White, M. 2013, ApJ, 775, 81

Rudie, G. C., Steidel, C. C., Trainor, R. F., et al. 2012, ApJ, 750, 67

Rykoff, E. S., Rozo, E., Busha, M. T., et al. 2014, ApJ, 785, 104

Saad, Y. 2003, Iterative methods for sparse linear systems (Siam)

Sijacki, D., & Springel, V. 2006, MNRAS, 366, 397

Skory, S., Hallman, E., Burns, J. O., et al. 2013, ApJ, 763, 38

Szabo, T., Pierpaoli, E., Dong, F., Pipino, A., & Gunn, J. 2011, ApJ, 736, 21

Takada, M., Ellis, R. S., Chiba, M., et al. 2014, PASJ, 66, 1

Viel, M., Haehnelt, M. G., & Springel, V. 2006, MNRAS, 367, 1655

Viel, M., Matarrese, S., Mo, H. J., Theuns, T., & Haehnelt, M. G. 2002, MNRAS, 336, 685

Vogelsberger, M., Genel, S., Sijacki, D., et al. 2013, MNRAS, 436, 3031

White, M. 2001, A&A, 367, 27

—. 2002, ApJS, 143, 241

White, M., Cohn, J. D., & Smit, R. 2010, MNRAS, 408, 1818

Wiener, N. 1949, Extrapolation, interpolation, and smoothing of stationary time series, Vol. 2 (MIT press Cambridge, MA)

Willick, J. A. 2000, ArXiv Astrophysics e-prints, astro-ph/0003232

Wilson, G., Muzzin, A., Yee, H. K. C., et al. 2009, ApJ, 698, 1943

Yang, H.-Y. K., Sutter, P. M., & Ricker, P. M. 2012, MNRAS, 427, 1614

Yuan, T., Nanayakkara, T., Kacprzak, G. G., et al. 2014, ApJ, 795, L20

APPENDIX

RECONSTRUCTION DERIVATION AND IMPLEMENTATION

In this appendix section we briefly review the Wiener filter, to establish our notation, and describe our efficient numerical algorithm for map making.

Wiener filter

We assume our data is made up of the signal we are interested in and additive noise $\mathbf{d} = \mathbf{s}_p + \mathbf{n}$. In order to keep coordinates clear, we use a p subscript to indicate 'pixel' coordinates, and an m subscript to indicate 'map' coordinates. Note that some other texts characterize this difference with the instrumental response matrix $\mathbf{R}$ as $\mathbf{s}_p = \mathbf{R}\mathbf{s}_m$. We want to make a linear estimate of the signal $\hat{\mathbf{s}} = \mathbf{L}\mathbf{d}$, with minimal error $\epsilon = E[|\mathbf{s}_m - \hat{\mathbf{s}}|^2]$. We start by simplifying the error expression.

$$\epsilon = \mathrm{tr}\left(E[\mathbf{s}_m\mathbf{s}_m^T] - E[\mathbf{s}_m\hat{\mathbf{s}}^T] - E[\hat{\mathbf{s}}\mathbf{s}_m^T] + E[\hat{\mathbf{s}}\hat{\mathbf{s}}^T]\right)$$

The first term $E[\mathbf{s}_m\mathbf{s}_m^T]$ is just the signal covariance $\mathbf{S}_{mm}$. The second term is

$$E[\mathbf{s}_m\hat{\mathbf{s}}^T] = E[\mathbf{s}_m(\mathbf{L}\mathbf{d})^T] = E[\mathbf{s}_m\mathbf{d}^T\mathbf{L}^T] = E[\mathbf{s}_m(\mathbf{s}_p^T + \mathbf{n}^T)\mathbf{L}^T]$$
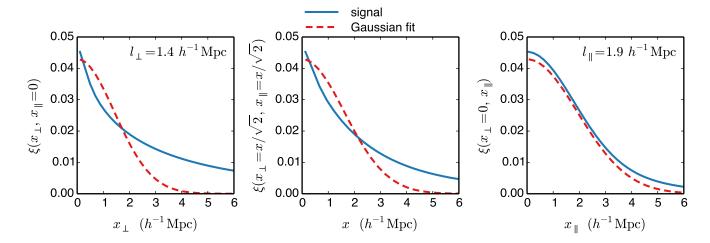$$= (E[\mathbf{s}_m\mathbf{s}_p^T] + E[\mathbf{s}_m\mathbf{n}^T])\mathbf{L}^T = \mathbf{S}_{mp}\mathbf{L}^T$$

FIG. 9.— The signal correlation function (solid line) compared to our assumed Gaussian form (dashed line), with amplitude, $l_\perp$, and $l_\parallel$ fit to the signal data.

since we assume $E[\mathbf{s}_m \mathbf{n}^T] = 0$. By a similar manipulation the third term $E[\hat{\mathbf{s}} \mathbf{s}_m^T] = \mathbf{L} \mathbf{S}_{pm}$. The fourth term is

$$E[\hat{\mathbf{s}} \hat{\mathbf{s}}^T] = \mathbf{L} E[\mathbf{d} \mathbf{d}^T] \mathbf{L}^T$$
$$= \mathbf{L}(E[\mathbf{s}_p \mathbf{s}_p^T] + E[\mathbf{s}_p \mathbf{n}^T] + E[\mathbf{n} \mathbf{s}_p^T] + E[\mathbf{n} \mathbf{n}^T]) \mathbf{L}^T$$
$$= \mathbf{L}(\mathbf{S}_{pp} + \mathbf{N}) \mathbf{L}^T$$

Altogether, the error is

$$\epsilon = \mathrm{tr} \mathbf{S}_{mm} - \mathrm{tr}(\mathbf{S}_{pm} \mathbf{L}^T) - \mathrm{tr}(\mathbf{L} \mathbf{S}_{mp}) + \mathrm{tr}(\mathbf{L}(\mathbf{S}_{pp} + \mathbf{N}) \mathbf{L}^T)$$
$$= \mathrm{tr} \mathbf{S}_{mm} - 2\mathrm{tr}(\mathbf{L} \mathbf{S}_{mp}) + \mathrm{tr}(\mathbf{L}(\mathbf{S}_{pp} + \mathbf{N}) \mathbf{L}^T)$$

Taking the derivative of the error with respect to the operator, we have

$$\frac{\partial \epsilon}{\partial \mathbf{L}} = -2 \mathbf{S}_{mp} + 2(\mathbf{S}_{pp} + \mathbf{N})^T \mathbf{L}^T$$

And then evaluating $\partial \epsilon / \partial \mathbf{L} = 0$ to find the minimum error, we have the optimal operator $\mathbf{L} = \mathbf{S}_{mp}(\mathbf{S}_{pp} + \mathbf{N})^{-1}$.

Signal covariance

The form we assume for the signal covariance is a product of two Gaussians, as shown in Equation 2. The flux correlation function should roughly have this form, but it is certainly not correct in detail. In this section, we consider the difference between the true signal covariance and our model (with appropriate $l_\perp$ and $l_\parallel$ values), and how this model inadequacy might affect our reconstruction results.

In Figure 9, we compare the correlation function of δ_F from the simulation (labeled signal) and our model fit to the ideal signal (labeled Gaussian fit). We have smoothed the signal along the line of sight to match a typical spectrograph resolution ($R \sim 1100$). From left to right, the three panels show different slices through the $(x_\perp, x_\parallel)$ plane, first all perpendicular, for $x_\perp = x_\parallel$, and for all parallel. We also annotated the fit Gaussian scales $l_\perp$ and $l_\parallel$. The Gaussian product shape does well along the line of sight, due to the fact that we have mocked the instrumental smoothing with a Gaussian filter, and the unsmoothed flux correlation is small for scales larger than the filter scale. Across the line of sight, our model does much worse. In a future iteration, we will consider using a sum of Gaussians... Such a mismatch between the simulation and model might be worrying, but we argue that this is not a concern for our application. In the case of Wiener filtering, most elements of the operator $\mathbf{S}(\mathbf{S} + \mathbf{N})^{-1}$ are close to 0 or 1, and the shape of $\mathbf{S}$ only changes values in the intermediate regime (see e.g. Press et al. 1992, for discussion).

In order to test the effect of an inaccurate covariance assumption on the reconstruction, we ran several reconstructions of the same pixel data, varying the signal covariance parameters $l_\perp$ and σ_F^2. The same slice from each reconstruction is shown in Figure 10. We vary $l_\perp$ from left to right and σ_F^2 from top to bottom. Overall, it appears that any reasonable changes to the parameter values (relative to the best-fit values) do not affect the morphology of the structures in the map. Increasing the flux variance increases the variance in the final map. This is due to the increase in all $\mathbf{S}$ elements relative to $\mathbf{N}$ so that pixels have larger weights in the reconstruction. That is, increasing the flux variance parameter should have the same effect as reducing all pixel noise estimates. Varying the correlation scale $l_\perp$ (or $l_\parallel$) has a more dramatic effect. With a fixed sightline sampling and a smaller correlation scale, the noise will obviously have a larger effect on the map, as the pixels are less correlated. As we increase the correlation scale, structures become increasing smoothed out. We found that changes in $l_\parallel$ behave the same as changes in $l_\perp$, so we did not add it to the plot.
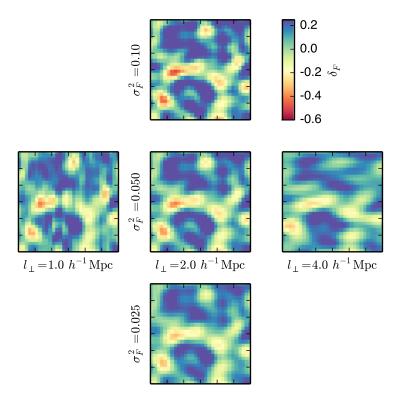
FIG. 10.— Slices through reconstructions run on the same pixel data, varying the signal covariance parameters $l_\perp$ and σ_F^2. The slices are $2\,h^{-1}$Mpc thick, projected over the x-axis (perpendicular to line of sight). The vertical axis of the images is along the line of sight. From left to right, we double the $l_\perp$ value, from 1 to 4. From bottom to top, we double the σ_F^2 value, from 0.025 to 0.1. Any reasonable deviations from the best case parameter values do not affect the morphology of the resulting map.

Numerical Implementation and Scaling

Computationally, the map making process consists of two steps. First, there is the matrix inversion and matrix-vector multiply $\mathbf{x} = \mathbf{A}^{-1}\mathbf{b} = (\mathbf{S}_{pp} + \mathbf{N})^{-1}\mathbf{d}$. The second step of the map process is just the multiplication $\mathbf{m} = \mathbf{S}_{mp}\mathbf{x}$. The matrix $\mathbf{A}$ is symmetric and positive definite, so there are several computationally efficient methods for obtaining the solution $\mathbf{x}$. Since our signal and noise matrices are both relatively sparse, we use the preconditioned conjugate gradient (PCG) method with a Jacobi pre-conditioner (Saad 2003) [3]. PCG is an iterative method which converges rapidly for sufficiently sparse matrices. For reasonable survey strategies, we do not expect a large number of pixels within a flux correlation scale (several Mpc), so methods that perform better for sparse matrices should be advantageous. We use the stopping condition that the residual is smaller than the norm of the data times a tolerance parameter, $|\mathbf{r}| = |\mathbf{b} - \mathbf{A}\mathbf{x}| < \mathrm{tol}|\mathbf{b}|$.

The real advantage of PCG for our problem, however, is that it never uses $\mathbf{A}$ directly, but only products of $\mathbf{A}$ and a vector. Since we know the functional form of $\mathbf{S}_{pp}$, and we assume $\mathbf{N}$ is diagonal, we do not have store the matrix $\mathbf{A}$, and instead compute elements when needed. This changes the space complexity of the algorithm from N_{pix}^2 to N_{pix}. For a typical problem where $N_{\mathrm{pix}} = 10^6$ the difference in storage is about $8\,\mathrm{TB}$ (for $\mathbf{A}$ stored in double precision), demanding several hundred nodes on modern systems, versus six vectors of length N_{pix}, requiring about $50\,\mathrm{MB}$ and easily fitting on a single node. Clearly, the performance of the PCG solve depends on how quickly we can compute elements of $\mathbf{A}$. We speed up the element lookup by using a small table of $\exp(x)$ for the Gaussian. This reduces each element lookup to 10 add/multiply operations.

Altogether, the cost of the reconstruction algorithm is $N_{\mathrm{lookup}}(N_{\mathrm{iter}}N_{\mathrm{pix}}^2 + N_{\mathrm{map}}N_{\mathrm{pix}})$, where N_{lookup} is the number of operations involved in computing elements of $\mathbf{A}$ and N_{iter} is the number of iterations before the PCG reaches the stop condition. We expect problem sizes of up to 10^6 pixels and 10^6 map points, so assuming 100 iterations, the calculation takes 10^{15} operations. This estimate indicates that we will likely not need to parallelize the code beyond shared memory, especially since the number of cores per node is expected to increase in coming years.

In order to choose a tolerance value for the PCG stop condition, we tested the PCG result against a direct Cholesky factorization for small problems. We generated a mock dataset with $N_{\mathrm{pix}} = 4000$, fixed the pixel positions and signal, and generated 10 noise realizations with SNR = 5. With multiple noise realizations, we can estimate the map variance due to noise compared to the error of the PCG solve. For each of the 10 noise realizations, we ran the reconstruction with the Cholesky solve and with the PCG solve with tol values of 1, 0.1, 0.01, and 10^{-3}. The Cholesky reconstruction

---

[3]   Also   see   `http://www.cs.cmu.edu/~quake-papers/`
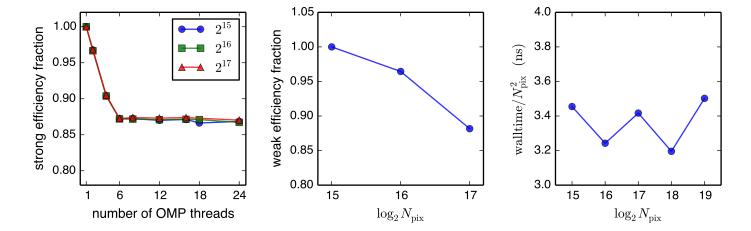`painless-conjugate-gradient.pdf`

FIG. 11.— Three scaling tests for our code. Left: 3 strong scaling tests, where we fix the problem size and increase the number of threads. As long as all threads are given enough work, the speedup should be linear. We show the efficiency $e_{\mathrm{strong}} = t_n/(nt_1)$ where n is the number of threads and the t is the walltime. Middle: a weak scaling test, where we fix the work per thread, increasing the problem size and number of threads. We show the efficiency $e_{\mathrm{weak}} = t_n/t_1$. Right: The element-wise time for several problem sizes.

took 18 seconds on average while the lowest tol PCG reconstruction took 0.9 seconds on average. The average number of PCG iterations to reach the various tol values were 5, 13, 29, and 37. We computed the standard deviation of the Cholesky map values over noise realizations σ_m to have a measure of the variance due to the noise at each map point. The average σ_m is 0.06 and the max is 0.11. We then computed the absolute difference of the PCG maps and Cholesky maps relative to the map noise std., $\epsilon = |\hat{s}_{\mathrm{PCG}} - \hat{s}_{\mathrm{Chol}}|/\sigma_m$. This error captures the fact that the PCG error must be smaller for map points with small noise variance. We found that the errors have an exponential distribution, with maximum values over all map points of 30, 4.5, 0.47, and 0.059 respectively for the 4 PCG tolerance settings. Since the max error of the tol = 0.01 PCG maps is less than unity and the error distribution is exponential, this tolerance setting is in the safe regime where the PCG residual error in the map is significantly smaller than the noise. In practice the PCG tol value should be adjusted for the problem at hand (if the SNR is very different), but this is a conservative choice for Lyα forest data in the near future.

One practical issue with the expressions in Equation 1 is that it does not easily allow for masking bad pixels. If we have any pixels with $n = \inf$, the PCG routine will return nan's. The ability to mask data is critical for Lyα forest data, where we may run into sky lines that add significant noise, or any pixels that should be masked entirely. We can rewrite the map expression using the fact that the noise covariance may be formed as a product of a lower triangular matrix with its transpose. In the case of our noise covariance, this $N_{ij} = (n_i \delta_{ik})(n_j \delta_{jk})^T$. It follows that

$$\mathbf{m} = \mathbf{S}_{mp}\mathbf{w}(\mathbf{w}\mathbf{S}_{pp}\mathbf{w} + \mathbf{I})^{-1}\mathbf{w}\mathbf{d} \tag{A1}$$

where $\mathbf{w} = \mathbf{n}^{-1}$. In this new expression, the matrix to be inverted is definite even for pixels with $w = 0$, and the PCG solves will work as expected. This expression requires more operations than the simpler Equation 1, but they add negligible overhead.

The reconstruction code implemented for this work consists of a static library and a few executables, written in C++, with no dependencies. The code can be compiled and run with no parallelism, but we recommend enabling OpenMP if available. The code is publicly available at `http://github.com/caseywstark/dachshund`, and includes some documentation and a test suite.

We performed scaling tests of our code to give an idea of what problem scale the code is able to handle within a reasonable wall time. We ran the test problems on the Edison machine at NERSC. Each Edison node has two 12-core Intel "Ivy Bridge" processors clocked at 2.4 GHz. We created mock surveys like the ones in Section 6 with an average sightline spacing of $\langle d_\perp \rangle = 2\,h^{-1}\mathrm{Mpc}$ and adjusted the volume to make problem sizes of $\log_2 N_{\mathrm{pix}} = 15$, 16, 17, 18, and 19. We ran the $\log_2 N_{\mathrm{pix}} = 15$, 16, and 17 problems with OMP_NUM_THREADS set to 1, 2, 4, 6, 8, 12, 16, 18, and 24. We set the number of threads to test the standard powers of two, but also included multiples of 6 to test the Edison NUMA boundaries, which have a significant effect.

In the first panel of Figure 11, we show the strong scaling efficiency (the walltime compared to what is expected for linear scaling) for these problems. We show the efficiency $e_{\mathrm{strong}} = t_n/(nt_1)$ where n is the number of threads and the t is the walltime for each run. The result is independent of the problem size. The relative speedup drops from 1.0 to 0.87 as the number of threads increases from 1 to 6, and then remains the same up to a full node. This suggests there is an increasing (but small) cost for threads to access memory until we hit the first NUMA barrier at 6 threads and is constant after that. In the middle panel, we show a weak scaling problem, increasing the number of threads from 1 to 4 to 16 as the problem size doubles (since the algorithm scales as N_{pix}^2). We show the efficiency $e_{\mathrm{weak}} = t_n/t_1$. The decrease in efficiency is similar to the strong scaling case, where the 16 thread case is 0.88 of the max efficiency. Finally, in the third panel we show the walltime per N_{pix}^2 element from problems all run with 24 threads, doubling

in size. The up-down pattern in this panel is not due to random system behavior, but instead the number of PCG iterations. The bottom runs took 12 iterations while the top took 13 due to small differences in the noise realizations. This test confirms the expected N_{pix}^2 scaling of the code and also demonstrates how fast the code is. If we consider the number of threads $n = 24$, the number of iterations $i = 12$, the clock speed $s = 2.4\,\text{ns}^{-1}$, and the element-wise time $t = 3.2\,\text{ns}$, the number of clock cycles taken per element per iteration is $nst/i = 15$. This is close to our estimate of 10 operations per lookup and multiply, even though the element-wise time measurement is an overestimate, including other operations like the $\mathbf{S}_{mp}\mathbf{x}$ multiply.

Error estimation

There are two possibilities for estimating the errors of the map values. First, we can compute the map covariance $\mathbf{M} = \mathbf{S}_{mp}(\mathbf{S}_{pp} + \mathbf{N})^{-1}\mathbf{S}_{pm}$ directly. This option is straightforward, but prohibitively expensive computationally. The inverse and product on the right of the map covariance is now a matrix instead of a vector, meaning we must run a PCG solve for each row of the solution matrix. One could also abandon an iterative method and perform a direct inverse. Either way, the computational complexity of the covariance calculation is a factor of N_{pix} greater than the map calculation. For any interesting problem, this is very expensive indeed.

Instead, we propose using Monte Carlo error estimation. We run n reconstructions on data with random noise realizations (consistent with the noise estimates), and estimate the map variance over the n results. We expect the required number of reconstructions n to be much smaller than N_{pix}, making this method much cheaper. For synthetic data sets, such as in this work, this method also allows us to test the effect of noise in the data and the effect of the sightline sampling independently.

Alternate smooth map construction

For our protocluster application, we are primarily interested in large-scale fluctuations. A simple way to pick out large-scale fluctuations is to smooth the field on the scale we are interested in, as we did earlier. This acts as a basic matched filter. However, instead of smoothing a high-resolution reconstruction, we could start with a different estimator that picks out large-scale fluctuations. We can think of our signal split into low and high-frequency components $\mathbf{s} = \mathbf{s}_l + \mathbf{s}_h$. The Wiener Filter estimate of the low-frequency signal is $\hat{\mathbf{s}}_l = (\mathbf{S}_{ll} + \mathbf{S}_{hl})(\mathbf{S} + \mathbf{N})^{-1}\mathbf{d}$. We can split the signal with a Gaussian filter $\mathbf{G}$ such that $\mathbf{s}_l = \mathbf{G}\mathbf{s}$ and $\mathbf{s}_h = \mathbf{s} - \mathbf{G}\mathbf{s}$. It follows that $\hat{\mathbf{s}}_l = \mathbf{S}\mathbf{G}(\mathbf{S} + \mathbf{N})^{-1}\mathbf{d}$. Compare this to the expression for a smoothed map, $\mathbf{G}\hat{\mathbf{s}} = \mathbf{G}\mathbf{S}(\mathbf{S} + \mathbf{N})^{-1}\mathbf{d}$. These expressions only differ by the position of the Gaussian filter, but it is an important distinction. In the case of the smoothed map, the filter acts on the map values, whereas in the case of the smooth signal reconstruction, the filter acts on the weighted pixel values. However, for any practical case where the filter scale is larger than the pixel and map spacing, these expressions will be very close to one another, and the distinction is no longer important.

OPTIMAL FILTER FOR PROTOCLUSTER SIGNAL

In this section, we explain a more advanced procedure for identifying protoclusters in the flux maps. We exploit the fact that we know the shape of the protocluster signal. We assume the flux map $d(\mathbf{x})$ is a combination of the protocluster signal and the background fluctuations of the Lyα forest. That is, $d(\mathbf{x}) = A\tau(\mathbf{x}) + \delta_F(\mathbf{x})$, where $\tau(\mathbf{x})$ is the shape of the protocluster profile and A is the strength of this signal.

In this case, the derivation of the optimal filter is shown in Appendix A of Haehnelt & Tegmark (1996), which we briefly review. We estimate the protocluster signal by convolving with a filter $\psi(\mathbf{x})$, so that $\hat{A} = \int \psi(\mathbf{x})d(\mathbf{x})d^3x$. The filter is normalized such that the estimate is unbiased, requiring $\int \psi(\mathbf{x})\tau(\mathbf{x})d^3x = 1$. In Fourier space, the unbiased, minimum variance estimator is then $\tilde{\psi}(\mathbf{k}) = C\tilde{\tau}(\mathbf{k})/P(\mathbf{k})$, where tildes indicate the Fourier transform of a quantity, $P(\mathbf{k})$ is the power spectrum of $\delta_F(\mathbf{x})$, and C is the normalization constant.

The optimal filter requires models for the protocluster profile and Lyα forest power spectrum. We model the protocluster profile as a Gaussian product parallel and perpendicular to the line of sight. This is similar to the data and model shown in Figure 4, although in this case we break spherical symmetry into the perpendicular and parallel components. We found that the average protocluster has a Gaussian σ scale of about $7\,h^{-1}\text{Mpc}$ perpendicular to the line of sight, and is reduced to about $4\,h^{-1}\text{Mpc}$ along the line of sight due to redshift-space distortions. We fit the Lyα forest power spectrum with a Kaiser and isotropic Gaussian-damped redshift-space power spectrum model, $P(k_\perp, k_\parallel) = ak^\alpha(1 + \beta k_\parallel^2/k^2)^2 \exp(-k^2\sigma^2)$. The normalization of the power is set by a combination of the bias of the Lyα forest the normalization of the primordial power spectrum. The k^α term accounts for a simple form of the primordial power spectrum scaling, which is sufficient for the scales in the simulation. The Kaiser term $(1 + \beta k_\parallel^2/k^2)$ handles the effects of redshift-space distortions on large scales. We include an isotropic, Gaussian damping term in order to capture suppression of small-scale fluctuations either due to pressure support or the smoothing effect of the Wiener filter. We found that the values $\alpha = -1.85$, $\beta = 1.07$, $\sigma = 2.06\,h^{-1}\text{Mpc}$ provided a good fit. The resulting filter, in configuration space, is shown Figure 12. It is encouraging to see a negative region in the plot of $\psi(x_\perp, x_\parallel)$. This means that the filter will naturally downweight modes which are dominated by background Lyα forest fluctuations. This is an improved filter compared to the 3D Gaussian filter used in the rest of the text, but we found that it did not make a significant difference in the candidate identification result.
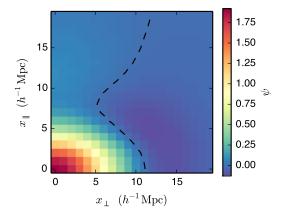
Fig. 12.— The optimal filter ψ in the $x_\perp, x_\parallel$ plane. The black dashed line shows the $\psi = 0$ contour.